Solar RRL
www.solar-rrl.com

Pyrene-Based Small-Molecular Hole Transport Layers for Efficient and Stable Narrow-Bandgap Perovskite Solar Cells

Paula Gómez, Junke Wang, Miriam Más-Montoya, Delia Bautista, Christ H. L. Weijtens, David Curiel, and René A. J. Janssen**

Lead–tin (Pb–Sn) hybrid perovskite materials possess ideal narrow bandgaps (1.2–1.4 eV) for efficient single-junction and tandem solar cells. Poly(3,4-ethylenedioxythiophene):polystyrene sulfonate (PEDOT:PSS) is commonly used as hole transport layer (HTL) for Pb–Sn perovskite solar cells (PSCs), despite its poor stability with these perovskites. Here, two new octacyclic heteroaromatic molecules, pyrenodiindole (PDI) and pyrenodi-(7-azaindole) (PDAI), are presented as the HTL for narrow-bandgap (1.23 eV) p–i–n Pb-Sn PSCs. The self-assembled reciprocal hydrogen-bonded solid-state structure of PDAI bestows robustness compared to PDI, making it less vulnerable in processing the perovskite film on top, and improves the reproducibility of device fabrication. Transient photocurrent measurements and light-intensity-dependent device characteristics indicate that PDI and PDAI possess similar hole extraction properties to PEDOT:PSS. As a result, similar open-circuit voltages and fill factors are obtained in the PSCs. Interestingly, the use of thin PDI and PDAI as HTL in PSCs changes the optical interference and reduces parasitic absorption in the near-infrared region, resulting in an improved short-circuit current density. Consequently, a higher power conversion efficiency of 16.1% is obtained for PDI and PDAI, compared to 15.1% for PEDOT:PSS. In addition, the self-assembled structure of PDAI led to a notable enhancement of device stability.

1. Introduction

Hybrid metal halide perovskites (AMX_3) have emerged as promising semiconductor materials for high-efficiency and low-cost photovoltaic (PV) devices. These perovskites are composed of a monovalent cation (A), a divalent metal cation (M), and a halide (X). The variation of the nature and ratio of the different components enables the tuning of the optoelectronic properties of the perovskite. Record power conversion efficiencies (PCEs) of up to 25.5% have been achieved using Pb-based perovskite solar cells (PSCs) with an optical bandgap of ≈1.5 eV.[1] Nevertheless, the toxicity of Pb ions makes it desirable to find alternative perovskite compositions that set the pace for an environmentally friendly photovoltaic technology without compromising the achievements in efficiency.[2] In the last few years, several options have been explored aiming at the replacement of Pb^{2+} with metals of similar ionic radii such as Ge^{2+}, In^{+}, Bi^{3+}, Sb^{3+}, and Sn^{2+}.[3] Recent developments on Sn-based PSCs offer pathways toward higher device performance due to the extended near-infrared absorption, low exciton binding energy, and good charge transport.[4] However, the high sensitivity of Sn^{2+} to oxidation, producing Sn^{4+}, causes self-doping and generates metal vacancies that deteriorate the perovskite layer and the device performance.[5] One of the current strategies consists in the partial substitution of Pb by Sn.[6] This approach presents the advantage that, along with the reduction of the Pb content, the combination of Pb and Sn narrows the bandgap to 1.2–1.4 eV, which is in the optimal range for single-junction devices in the Shockley–Queisser limit.[7] In addition, such a

P. Gómez, M. Más-Montoya, D. Curiel
Multifunctional Molecular Materials
Department of Organic Chemistry
Faculty of Chemistry
University of Murcia
Campus of Espinardo, Murcia 30100, Spain
E-mail: davidcc@um.es

The ORCID identification number(s) for the author(s) of this article can be found under https://doi.org/10.1002/solr.202100454.

DOI: 10.1002/solr.202100454

J. Wang, C. H. L. Weijtens, R. A. J. Janssen
Molecular Materials and Nanosystems
Institute for Complex Molecular Systems
Eindhoven University of Technology
Eindhoven 5600 MB, The Netherlands
E-mail: r.a.j.janssen@tue.nl

D. Bautista
Scientific Instrumentation Service
University of Murcia
Murcia 30100, Spain

R. A. J. Janssen
Dutch Institute for Fundamental Energy Research
Eindhoven 5612 AJ, The Netherlands

narrow bandgap is also suitable for developing all-perovskite tandem solar cells.[8]

To date, the efficiency of the best Pb–Sn hybrid perovskite devices (20–21%) still lags behind that of their Pb counterparts, but they show continuous and promising progress.[9] Among the different strategies investigated for optimizing mixed Pb–Sn perovskite solar cells, most have focused on engineering the active layer by modifying the film processing methodology and adjusting the perovskite composition. In this regard, a detailed study of the Pb:Sn ratio[10] or the use of diverse additives[11] has demonstrated to be useful to increase device efficiency. It is curious that despite the unquestionable role that interfacial layers have played in the progress of conventional Pb-based perovskite solar cells, very little attention has been paid to their investigation in mixed Pb–Sn devices. Nevertheless, their involvement in the charge extraction processes and their protective function are essential features for the optimum performance and long-term stability of the solar cell. As far as the hole transporting layers (HTLs) are concerned, the small ionization potential of Pb–Sn perovskite can represent a limiting factor for interfacial materials requiring a suitable energy level alignment to be inserted between the perovskite layer and the electrode.[12] Currently, poly(3,4-ethylenedioxythiophene):polystyrene sulfonate (PEDOT:PSS) is the most frequently used HTL in Pb–Sn hybrid devices with an inverted p–i–n architecture.[12b] However, PEDOT:PSS presents some drawbacks that make its adequacy as HTL questionable. Its acidity causes unwanted reactions with the perovskite layer that induce device degradation. Analogously, the sensitivity of perovskite solar cells to humidity advises against using a hygroscopic HTL such as PEDOT:PSS. The poor thermal stability of PEDOT:PSS leads to a charge extraction barrier upon aging.[12a] Moreover, the PEDOT:PSS layer also causes parasitic absorption in the near-infrared region, which would reduce the photocurrent of the narrow-bandgap subcell in a tandem device.[13]

So far, very few examples of alternative HTLs have been described for Pb–Sn perovskite devices and most of them are based on PEDOT:PSS engineering. In this regard, the integration of ultrathin bulk-heterojunction organic semiconductors (PBDB-T:ITIC) between PEDOT:PSS and the narrow-bandgap perovskite has been reported.[14] The incorporation of these materials formed a gradient band alignment and, in addition, had a passivation effect on the surface traps that led to highly efficient $(FASnI_3)_{0.6}(MAPbI_3)_{0.4}$ (FA is formamidinium, MA is methylammonium) devices. PEDOT:PSS has also been modified with a perfluorinated ionomer (NAFION, tetrafluoroethylene-perfluoro-3,6-dioxa-4-methyl-7-octenesulfonic acid copolymer), which increased the work function of pristine PEDOT:PSS.[15] This led to a better energy-level alignment with the mixed Pb–Sn perovskite that improved the open-circuit voltage (V_{OC}) and, in consequence, the PCE. Another modification consisted in building a bilayer structure where the combination of CuI and PEDOT:PSS improved the short-circuit current density (J_{SC}) and fill factor (FF) when compared to single HTL devices.[16] One of the few examples of replacing PEDOT:PSS has been reported for devices based on $FAPb_{0.5}Sn_{0.5}I_3$, synthesized via thermal coevaporation of precursors, which used an indium tin oxide (ITO) contact coated with MoO_3 followed by the deposition of poly[bis(4-phenyl)(2,4,6-trimethylphenyl)amine] (PTAA) as HTL.[17] In another example, an anionic conjugated polymer with alkylsulfonate side groups (PCP-Na) was used with a solution-processed $FAPb_{0.5}Sn_{0.5}I_3$ perovskite to provide a higher V_{OC} and FF than PEDOT:PSS.[18]

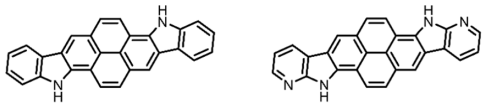

Figure 1. Chemical structures of PDI and PDAI.

Motivated by this context, we report the use of conjugated small molecules, based on self-assembled azapolyheteroaromatics (**Figure 1**), as HTL for narrow-bandgap mixed Pb–Sn perovskite solar cells. Recently, we reported that anthradi-7-azaindole (ADAI) as a non-doped HTL can effectively replace PEDOT:PSS in inverted $MAPbI_3$ solar cells.[19] ADAI self-assembles in the solid state forming an interfacial layer that improved the morphology of the perovskite layer and reduced nonradiative recombination in $MAPbI_3$-based devices. The distinctive feature of ADAI's molecular design is based on the integration of hydrogen bond donor and acceptor sites within the conjugated skeleton via the condensation of the 7-azaindole building block. The rational location of these sites in a centrosymmetric structure promotes the molecular self-assembly via reciprocal hydrogen bonding. We demonstrated that, as a consequence, ADAI exhibits a significant robustness that substantiates a consistent performance as hole transporting material.[20] Based on these antecedents, the hydrogen-bonded network becomes an appealing structural motif that could further contribute to the protection of the active layer and the stability of solar cells. Therefore, we synthesized molecular materials in which we extend the π-conjugated core from anthracene as used in ADAI to pyrene. Subsequent double condensation of two 7-azaindole units results in pyrenodi-(7-azaindole) (PDAI), which has a narrower energy gap between the highest occupied and lowest unoccupied molecular orbitals (HOMO and LUMO) than ADAI and shows a good energy-level alignment with a narrow-bandgap $FA_{0.66}MA_{0.34}Pb_{0.5}Sn_{0.5}I_3$ perovskite. To investigate the effect of the hydrogen-bond-directed self-assembly on the properties of the HTL, an analogous octacyclic molecule, pyrenodiindole (PDI) that cannot form reciprocal hydrogen bonds has been synthesized and investigated. Interestingly, both materials outperform PEDOT:PSS as HTL by increasing J_{SC} due to the changes of optical interference and reduced parasitic absorption in narrow-bandgap PSCs. Importantly, a remarkable improvement in the device stability has been obtained when using the self-assembled PDAI as HTL.

2. Results and Discussion

The synthetic route for the molecules PDI and PDAI is shown in **Scheme 1**. Initially, a double palladium-catalyzed Buchwald–Hartwig[21] cross-coupling reaction between 1,6-diaminopyrene[22] and the corresponding dihaloderivative,

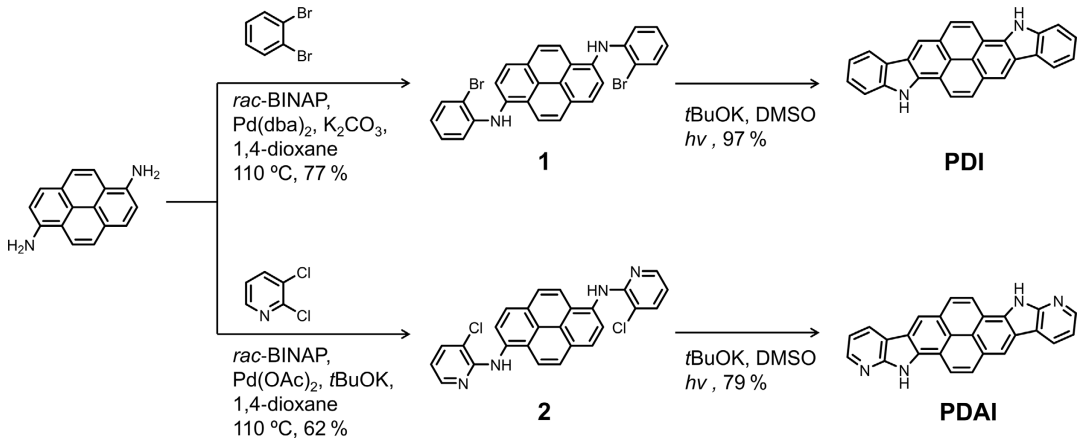

Scheme 1. Synthetic routes of PDI and PDAI.

o-dibromobenzene or 2,3-dichloropyridine, leads to the formation of the *N*-arylated intermediates **1** and **2**, respectively. Subsequently, a photoinduced regiospecific double intramolecular cyclization between the C—X (X = Cl or Br) carbons in the peripheral aromatic rings and the carbons in the positions 2 and 7 of the pyrene unit affords the desired polyheteroaromatic systems PDI and PDAI.[23] The structures of the intermediate and final products were unequivocally characterized by nuclear magnetic resonance and high-resolution mass spectrometry. All the details can be found in the Supporting Information (Figure S1–S4, Supporting Information). To improve the purity of the materials to be used as HTLs, they were purified by gradient sublimation under high-vacuum conditions.

The optical characterization of PDI and PDAI was performed by UV–vis absorption spectroscopy in *N,N*-dimethylformamide (DMF) solution and in the solid state as thin films deposited on quartz substrates (**Figure 2**). Both materials display similar vibrational fine structure in solution and their spectra are mostly located in the UV region with a small absorption in the lower wavelength limit of the visible region. In thin films broader

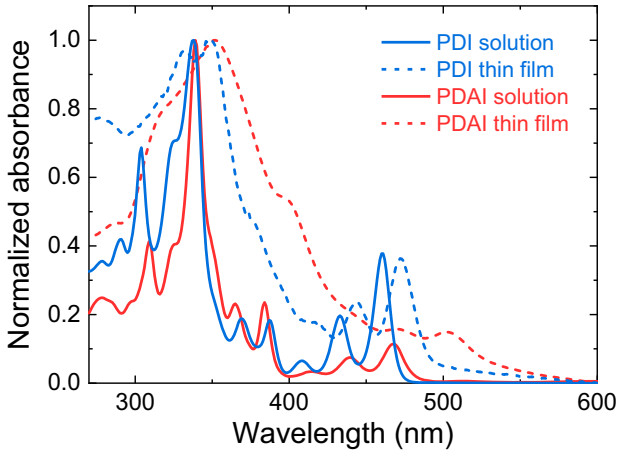

Figure 2. Normalized absorption spectra of PDI and PDAI in DMF solution (2.5×10^{-5} M) (solid lines) and as a thin film on the quartz substrate (dashed lines).

Table 1. Optical properties and frontier orbital energies.

	λ_{max}^{sol} [nm]	λ_{max}^{film} [nm]	E_g^{film} [a] [eV]	E_{onset}^{ox} [b] [V]	E_{HOMO}^{CV} [c] [eV]	E_{LUMO}^{CV} [d] [eV]	E_{HOMO}^{DFT} [e] [eV]	E_{HOMO}^{UPS} [f] [eV]
PDI	460	472	2.53	0.93	−5.35	−2.82	−4.81	−5.02
PDAI	468	502	2.32	1.12	−5.54	−3.22	−4.97	−4.89

[a]Bandgap estimated from the absorption onset; [b]Versus Ag/AgCl; [c]From CV: $E_{HOMO}^{CV} = -(4.8 + E_{onset}^{ox} - E_{onset\,Fc/Fc+}^{ox})$; [d]Estimated from $E_{LUMO}^{CV} = E_{HOMO}^{CV} + E_g^{film}$; [e]From DFT; [f]From UPS.

and bathochromically shifted spectra were obtained as a result of the intermolecular interactions gaining relevance in the solid state. The optical bandgaps were determined for PDI and PDAI from the onset of the low-energy absorption (**Table 1**). The molecules have limited absorption in the visible region and in thin layers will hardly interfere with the sunlight absorption.

The HOMO energies (E_{HOMO}^{CV}) were estimated from the onsets of the oxidation waves (E_{onset}^{ox}) via cyclic voltammetry (CV) on thin PDI and PDAI films (Figure S5, Supporting Information), resulting in −5.35 eV for PDI and −5.54 eV for PDAI (Table 1). The LUMO energies (E_{LUMO}^{CV}) were estimated by adding the optical bandgaps (E_g^{film}) to E_{HOMO}^{CV}. The deeper HOMO energy for PDAI reflects the electron-withdrawing effect of the pyridine rings. Density functional theory (DFT) calculations confirm the effect of the electron-withdrawing pyridines in a map of the electrostatic potential, which is positive near the nitrogen atoms of pyrrole but negative near those of pyridine (Figure S6, Supporting Information). The ionization potentials (IPs) estimated by DFT are 4.81 eV for PDI and 4.97 eV for PDAI. Using ultraviolet photoelectron spectroscopy (UPS) (Figure S7a, Supporting Information), we find that the IPs amount to 5.02 eV for PDI and 4.89 eV for PDAI for ≈15 nm films on ITO. The IPs measured by UPS depend somewhat on film thickness (Figure S7b, Supporting Information). The HOMO energies obtained by UPS are less deep than those obtained by CV (Table 1). Moreover, the HOMO energy determined by UPS is deeper for PDI than for PDAI, which is unexpected considering the electron-deficient pyridine rings of PDAI.

Although intermolecular interactions and molecular orientation can affect the ionization potential in thin molecular films,[24] there is at present no simple explanation for the observed differences in IP between CV, DFT, and UPS but, independently of the method used for the determination of the electronic structure of the HTLs, both PDI and PDAI show a suitable gradient in the alignment of the energy levels with the adjacent materials (**Figure 3**) and fulfill the requirements for their incorporation in the solar cell architecture. For PEDOT:PSS, the IP is 5.06 eV.[25] The energy of the valence band edge for the Pb–Sn mixed perovskite determined by UPS is −5.58 eV. The conduction band edge of the low-bandgap Pb–Sn perovskite is estimated at −4.35 eV and therefore the LUMO energies determined for PDI and PDAI are high enough for these materials to act as electron blocking layers. The energy diagram using these and previous published values for C_{60}[26] and BCP[27] is shown in Figure 3.

The thermal stability of the materials was studied by thermogravimetric analysis (Figure S8, Supporting Information), which showed that both molecules have high decomposition temperatures (corresponding to a 5% weight loss), 443 °C for PDI and 534 °C for PDAI. The significantly higher thermal stability of PDAI is attributed to the robustness bestowed by the hydrogen-bond-directed self-assembly controlled through the strategically located 7-azaindole substructures. These enable the integration of hydrogen bond donor sites (pyrrole-NH) and hydrogen bond acceptor sites (pyridine-N) within the fused polyheteroaromatic system itself. The intermolecular hydrogen bonding was further corroborated by Fourier transform infrared (FT-IR) spectroscopy of the solid materials. A notable shift of the N—H stretch vibration to lower wavenumbers, consistent with hydrogen bond formation, is evident when comparing the spectra of PDI (3425 cm^{-1}) and PDAI (3135 cm^{-1}) (Figure S9, Supporting Information).

Structural characterization by X-ray diffraction experiments provide an insight into the effect of the molecular structure on the solid state packing. Both pyrene-based octacyclic structures are virtually flat. PDI crystallizes in a monoclinic lattice (space group $P2_1/n$) where each molecule is in van der Waals contact with six neighboring molecules. Some of them set π–π interactions and pack in parallel planes forming a slipped stack arrangement with an interplanar distance of 3.14 Å (**Figure 4**a).

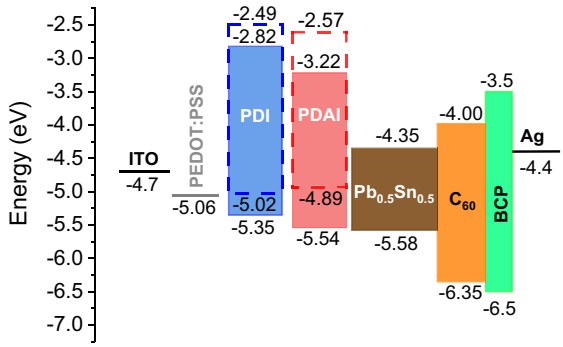

Figure 3. Energy-level diagram for the solar cell configurations with the three different HTLs (PEDOT:PSS, PDI, and PDAI). For PDI and PDAI, the colored bars are based on CV; the dashed-lined colorless bars are based on UPS.

In addition, edge-to-face interactions (C—H···π, 2.86 Å) connect the molecules packed in almost orthogonal planes (86.1°). When the crystal network is expanded, a herringbone pattern can be recognized (Figure 4b). Interestingly, different from the typical herringbone arrangement, where edge-to-face interactions are commonly set through the long molecular edge, in this particular case these interactions are established through the short edge of the PDI molecule. On the other hand, PDAI crystallizes in a monoclinic unit cell (space group C2/c) and the substitution of the peripheral benzene rings by pyridine rings led to a completely different solid state packing governed by reciprocal pyrrole-NH···N-pyridine hydrogen bonds (2.27 Å). The centrosymmetric structure of PDAI facilitates the formation of ribbon-like structures stabilized by four hydrogen bonds that produce a supramolecular expansion of the π-conjugated surface (Figure 4c). Consequently, π–π interactions are favored and promote the packing of molecules in parallel ribbons that define a slipped columnar arrangement. Edge contacts between molecules packed in neighboring ribbons reveal that in the expanded structure the adjacent columnar packing adopts different directions, leading to a robust crystalline network (Figure 4d).

Grazing-incidence wide-angle X-ray scattering (GIWAXS) measurements were performed for thin films, thermally evaporated onto ITO/glass substrates (Figure S10, Supporting Information). For PDI diffraction peaks are present in the out-of-plane direction at q_z = 0.43 and 0.48 $Å^{-1}$, whereas for PDAI there is one diffraction peak at q_z = 0.67 $Å^{-1}$ and a diffuse π stacking peak at q_z ≈1.8–1.9 $Å^{-1}$. The diffraction intensity in the in-plane direction is very low for both compounds. These results indicate that evaporated PDI and PDAI films are semicrystalline and have some preferential orientation.

Thin films deposited on ITO substrates were also characterized by X-ray photoelectron spectroscopy (XPS). The signal ascribed to the N 1*s* core level confirmed the presence of two different nitrogen atoms at the surface in the as-deposited PDAI, where the deconvoluted peaks at 399 and 400 eV can be assigned to the pyridinic and pyrrolic nitrogen atoms, respectively (**Figure 5**).[28] In agreement with the structure of PDI, only the pyrrolic nitrogen at 400 eV was observed (Figure 5a). With the aim of mimicking the solution processing used for depositing the Pb–Sn perovskite films, both substrates were washed with DMF. As a result, both the C 1*s* and N 1*s* XPS signals of PDI thin films are significantly reduced (Figure 5a,c). Contrariwise, the PDAI layer was largely retained on the substrate after DMF washing, showing that it is more robust under the experimental conditions used for the device fabrication (Figure 5b,d). UV–vis absorption spectra (Figure S11, Supporting Information) confirm this difference between PDI and PDAI. A substantial decrease of absorbance is seen for the DMF-rinsed PDI layer, whereas the PDAI layer shows less reduction (Figure S11, Supporting Information). Thermal annealing (100 °C, 10 min) provided no significant improvement in robustness against processing of DMF on top of these materials.

The performance of ultrathin PDAI and PDI HTLs in planar p–i–n PSCs was evaluated in a LiF/glass/ITO/HTL/perovskite/C_{60}/BCP/Ag device structure. The LiF layer was thermally evaporated as antireflection coating.[12b] PDAI and PDI were

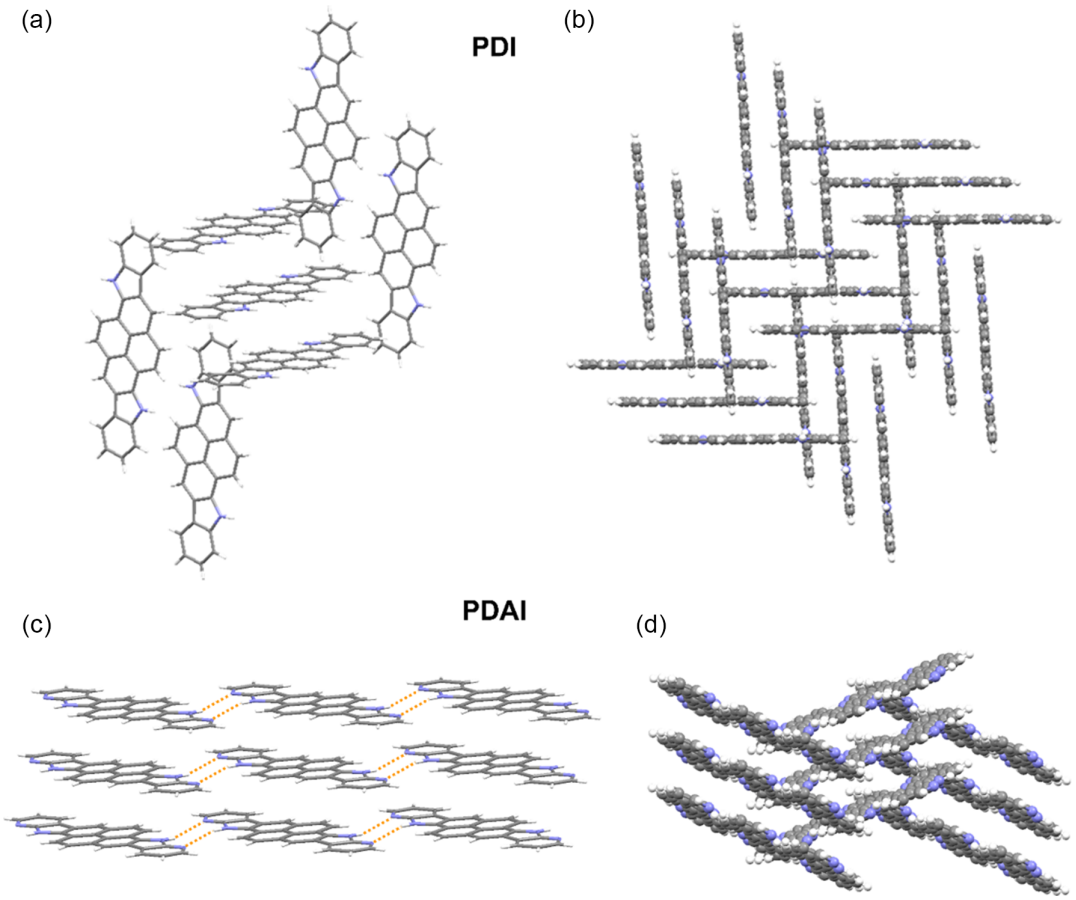

Figure 4. X-ray structures of a,b) PDI and c,d) PDAI. Solvent molecules have been omitted in the structure of PDI for the sake of clarity. Orange dotted lines represent hydrogen bonds.

deposited on top of the ITO substrate via thermal evaporation (≈10 nm, after optimization) and compared with a solution-processed PEDOT:PSS layer (≈50 nm). $FA_{0.66}MA_{0.34}Pb_{0.5}Sn_{0.5}I_3$ was deposited by a two-step solution process and had a bandgap of 1.23 eV.[29] The formation of narrow-bandgap perovskite films is not affected by the HTL. Top-view scanning electron microscope (SEM) images of the $FA_{0.66}MA_{0.34}Pb_{0.5}Sn_{0.5}I_3$ films deposited on PEDOT:PSS, PDI, and PDAI (**Figure 6**a–c) show compact and pinhole-free surface morphologies with a comparable mean grain size of around 450 nm (Figure S12, Supporting Information). The UV–vis–NIR absorption spectra of these films are very similar with a characteristic narrow-bandgap onset around 1000 nm (Figure 6d). X-ray diffraction (XRD) (Figure 6e) indicates that in each case the perovskite adopted the same cubic structure because the same set of crystallographic planes are detected, despite the sample on PDAI showing slightly lower peak intensities.

Figure 7a shows the stabilized current density–voltage (J–V) curves of the best-performing PSCs with PEDOT:PSS, PDI, and PDAI as HTLs. The external quantum efficiency (EQE) spectra and device parameters are displayed in Figure 7b and **Table 2**, respectively. It is found that the control device with PEDOT:PSS exhibits a PCE of 15.1%, with a J_{SC} of 27.6 mA cm^{-2} (corrected by EQE), a V_{OC} of 0.77 V, and a FF of 0.71. For PSCs with PDAI and PDI, comparable V_{OC} and FF are obtained while the J_{SC} is improved by 1.5 to 29.1 mA cm^{-2}, according to the integration of EQE spectra. The EQE spectra indicate that the enhanced J_{SC} is due to an increase of the spectral response in the 300–400, 500–700, and 850–950 nm regions. As a result, the devices fabricated with PDAI and PDI exhibit higher PCEs with a value of 16.1%. The PCEs from J–V characteristics are also confirmed by steady-state power output tracking (Figure 7c), in which the devices with PDAI and PDI are performing better than that with PEDOT:PSS. All devices show very small hysteresis between downward and upward scans (Figure S13, Supporting Information). Notably, the dark J–V curves suggest that the device based on PDAI has a lower leakage current density than the PDI (Figure 7d), attributed to the better robustness of PDAI on the ITO substrate against solution processing.

Figure S14, Supporting Information, shows box plots of the statistical distribution of performance characteristics of PSCs with PEDOT:PSS, PDI, and PDAI. Whereas the control device with PEDOT:PSS exhibits an average PCE of 14.2 ± 2.2%, devices with PDI have a much broader spread in the performance (10.0 ± 5.5%), most likely due to the higher susceptibility and partial dissolution of PDI layers for perovskite precursor solutions. In comparison, devices with PDAI display similar average PCEs (13.8 ± 2.05%) as those obtained with PEDOPT:PSS.

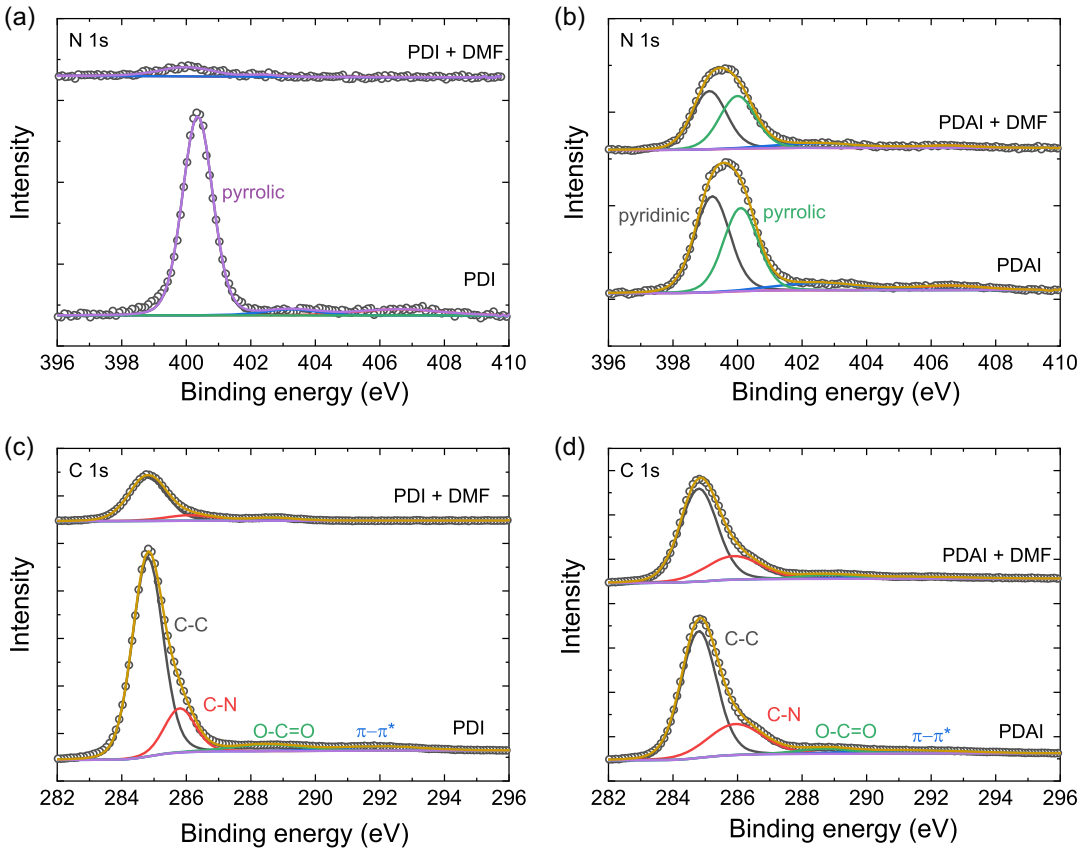

Figure 5. XPS high-resolution scan spectra of the a,b) N 1s and c,d) C 1s core levels for (a,c) PDI and (b,d) PDAI thin films before and after DMF washing.

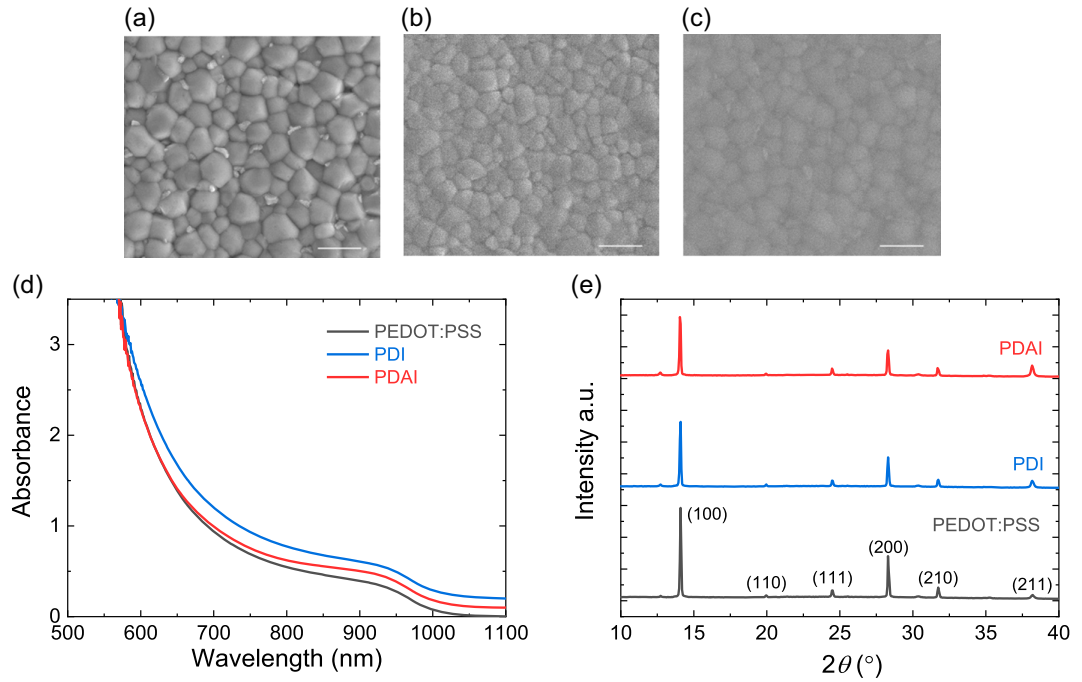

Figure 6. Top-view SEM images of deposited $FA_{0.66}MA_{0.34}Pb_{0.5}Sn_{0.5}I_3$ films. a) On PEDOT:PSS. b) On PDI. c) On PDAI. Scale bars are 1 µm. d) UV–vis–NIR absorption spectra of $FA_{0.66}MA_{0.34}Pb_{0.5}Sn_{0.5}I_3$ deposited on different HTLs. The spectra are offset vertically by 0.1 OD to enable comparison. e) XRD patterns of $FA_{0.66}MA_{0.34}Pb_{0.5}Sn_{0.5}I_3$ deposited on different HTLs.

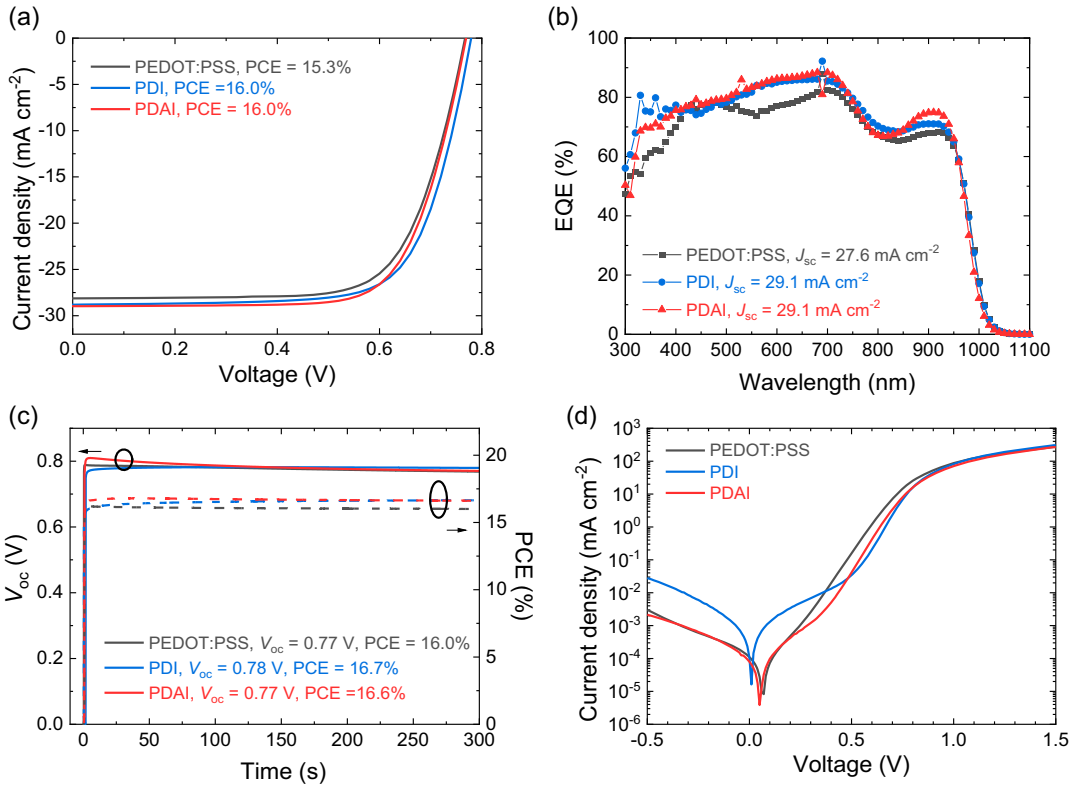

Figure 7. Device characteristics of $FA_{0.66}MA_{0.34}Pb_{0.5}Sn_{0.5}I_3$ solar cells using PEDOT:PSS, PDI, and PDAI as HTL. a) Stabilized *J–V* curves. b) EQE spectra measured under 940 nm bias light. c) V_{OC} and PCE tracking. d) Dark *J–V* curves.

Table 2. Photovoltaic parameters of representative narrow-bandgap PSCs with PEDOT:PSS, PDI, or PDAI as HTL.

HTL	J_{SC} [mA cm^{-2}]	V_{OC} [V]	FF	PCE [%]	$J_{SC,\ EQE}$ [mA cm^{-2}]	PCE[a)] [%]
PEDOT:PSS	28.1	0.77	0.71	15.3	27.6	15.1
	27.5 ± 0.69	0.74 ± 0.07	0.69 ± 0.07	14.2 ± 2.2		
PDI	28.8	0.78	0.71	16.0	29.1	16.1
	24.29 ± 6.74	0.64 ± 0.18	0.58 ± 0.16	10.0 ± 5.5		
PDAI	29.0	0.77	0.72	16.0	29.1	16.1
	28.17 ± 1.01	0.73 ± 0.05	0.67 ± 0.06	13.8 ± 2.1		

[a)]Corrected PCE obtained by calculating the J_{SC} integrated from the EQE spectrum and V_{OC} and FF from the stabilized *J–V* measurement.

Thermal annealing (100 °C, 10 min) of PDI and PDAI prior to depositing the perovskite layer improves the reproducibility, but results in a slightly reduced record PCE (Figure S14d, Supporting Information).

The EQE spectra (Figure 7b) indicate an increased J_{SC} by 1.5 mA cm^{-2} after replacing the thick PEDOT:PSS layer (≈50 nm) by ultrathin PDI or PDAI HTLs. The equal improvement of the EQE in specific spectral regions for PDI and PDAI compared to PEDOT:PSS suggests that the J_{SC} enhancement is possibly due to an optical effect. To assess this explanation, the fraction of photons absorbed by the narrow-bandgap perovskite in the device was estimated using the transfer-matrix model for 50 and 5 nm thick HTLs. The simulations reveal that replacing the 50 nm thick PEDOT:PSS layer with a 5 nm HTL indeed improves the fraction of absorbed photons considerably in specific regions of the spectrum (Figure S15, Supporting Information). Constructive interference and reduced parasitic absorption in the NIR region contribute to the increased fraction of absorbed photons. To experimentally confirm the optical effect, we fabricated perovskite devices based on ≈5 and 50 nm thick PEDOT:PSS HTLs. The thin PEDOT:PSS layer was prepared by adding water dropwise onto a spinning PEDOT:PSS substrate.[30] For solar cells prepared in the same batch (Figure S16, Supporting Information), we found that both

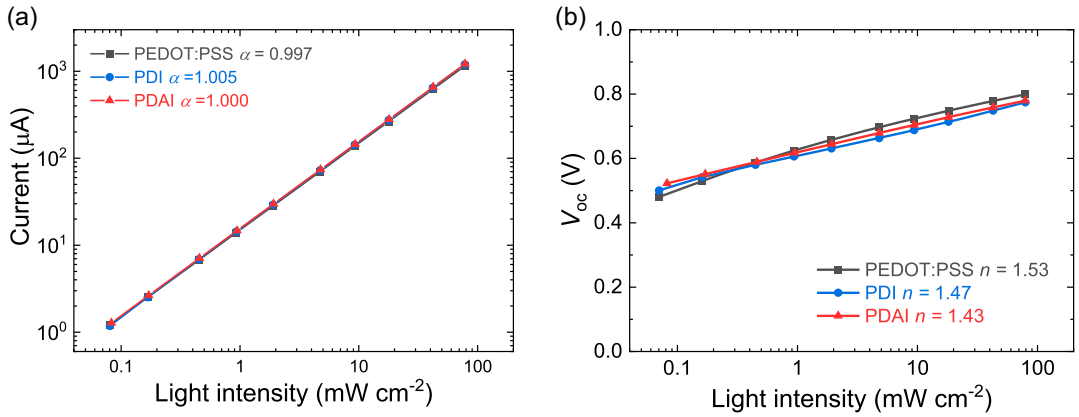

Figure 8. Light-intensity dependence of a) I_{SC} and b) V_{OC} of PSCs with different HTLs. A 730 nm LED was used as the light source.

devices exhibit a comparable V_{OC} and FF. Interestingly, an enhancement in the J_{SC} of 2.1 mA cm^{-2} was observed for the thin PEDOT:PSS-based device, which shows an EQE spectrum that is similar to that of PDI and PDAI devices. The results demonstrate that the ultrathin PDI and PDAI HTLs are beneficial to the J_{SC}.

The energy-level offset between the charge transport layers and the perovskite can drastically increase the rate of interface recombination and hence limit the maximum attainable V_{OC}.[31] The fact that the cells with different HTLs show a similar V_{OC} suggests that the narrow-bandgap devices are not limited by differences in nonradiative recombination at the perovskite/HTL interfaces. Additional information about the charge extraction and recombination were obtained from measuring the light intensity (I) dependence of J_{SC} and V_{OC}. **Figure 8**a reveals a linear relationship ($J_{SC} \propto I^{\alpha}$, where $\alpha \approx 1$), which demonstrates that there are no significant energy barriers or space charges to limit the charge extraction process in such devices at short circuit.[32] The light-intensity dependence of V_{OC} measurements (Figure 8b) shows slight differences in the light-ideality factor (determined from the slope of the V_{OC} versus the logarithm of the light intensity over k_BT, where k_B is the Boltzmann constant). The deviation of the ideality factor from the value of 1 can be interpreted as a contribution of Shockley–Read–Hall (SRH) recombination. The values obtained for the different HTLs suggest that the devices have similar recombination mechanisms.[33]

To study the charge extraction, we performed transient photocurrent measurements by applying a 50 μs square pulse of monochromatic excitation (543 nm LED) to the device (0 V, dark condition) while monitoring its temporal photocurrent response. As shown in **Figure 9**a, the three devices display a fast rise and stabilization of the photocurrent within a few microseconds after turning on the illumination, suggesting a rapid trap-filling process in the solar cells.[32] After turning off the illumination, a comparably fast decay process is observed, and the charge transit time is found to be 0.90 μs for PDAI, and 0.96 μs for both PEDOT:PSS and PDI. Accordingly, the vertical charge carrier transit mobility[34] is determined to be 2.6, 2.7, and 2.9×10^{-3} cm^2 V^{-1} s^{-1} for devices with PEDOT:PSS, PDI, and PDAI, respectively. The results indicate that charge extraction by PDI and PDAI is similar to that of PEDOT:PSS.

The degree of electronic disorder of the perovskite films deposited onto the different HTLs was determined from the

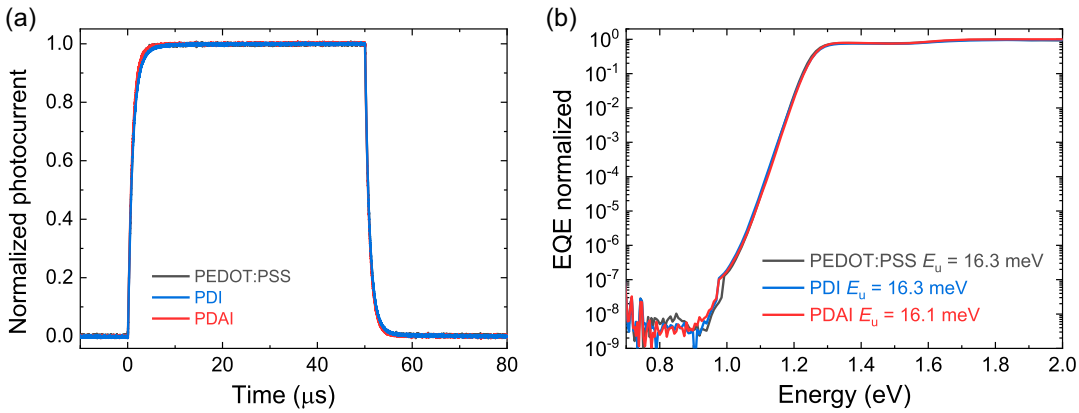

Figure 9. a) Short-circuit photocurrent measured with 50 μs square-pulse illumination. b) Sub-bandgap EQE spectra for the PSCs based on PEDOT:PSS, PDI, and PDAI HTLs.

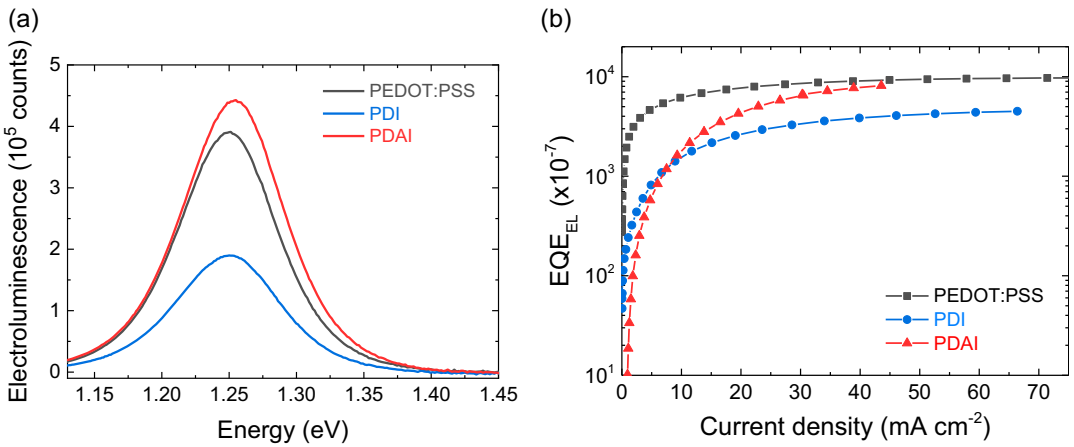

Figure 10. a) Electroluminescence spectra of $FA_{0.66}MA_{0.34}Pb_{0.5}Sn_{0.5}I_3$ PSCs with PEDOT:PSS, PDI, or PDAI as HTL. b) Corresponding external electroluminescence quantum efficiency as function of current density.

Urbach energy (E_u) obtained by fitting the tail of the EQE spectra in the sub-bandgap region (Figure 9b). The E_u is 16.2 ± 0.1 meV for all three devices, suggesting a similar semiconductor quality of $FA_{0.66}MA_{0.34}Pb_{0.5}Sn_{0.5}I_3$ films when deposited on PEDOT:PSS, PDI, and PDAI.[35] Other than this Urbach tail, no defect-related transitions are observed in the sub-bandgap region.

The electroluminescence (EL) spectra of the cells with the three different HTLs were measured and the external EL quantum efficiency was estimated (**Figure 10**). The EL maximizes at 1.25 eV. The EQE_{EL}s at a forward current density of $J = 30\ mA\ cm^{-2}$ (close to J_{SC} in Table 2) of 8.6×10^{-4} (PEDOT:PSS), 3.4×10^{-4} (PDI), and 6.4×10^{-4} (PDAI) are within a close range and suggest voltage losses ($\Delta V_{OC} = (k_B T/q)\ln(EQE_{EL})$) of 0.19 to 0.21 V. At the bandgap of 1.23 eV, the V_{OC} in the radiative limit ($V_{OC,rad}$) is about 0.97 V,[7] and after subtracting ΔV_{OC}, the estimated V_{OC} is 0.77 ± 0.01 V, in excellent agreement with the experimental values from the J–V characteristics measured under simulated AM 1.5G illumination (Table 2).

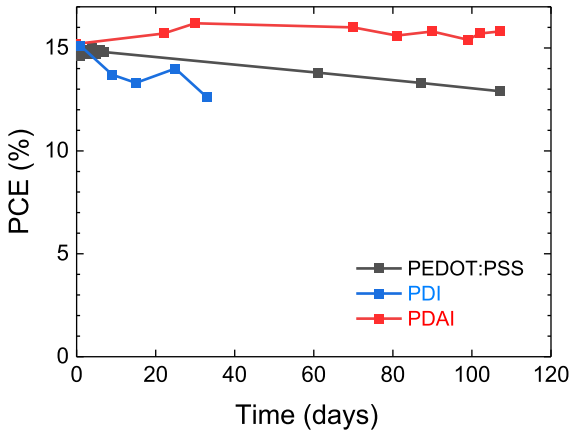

Figure 11. PCE of unencapsulated PSCs based on PEDOT:PSS, PDI, and PDAI upon storage in the N_2 atmosphere at room temperature.

Finally, the device stability was monitored by tracking the PCE of the solar cells stored in dry N_2 atmosphere in the dark at room temperature (**Figure 11**). During the tracking period, the PEDOT:PSS-based devices exhibited a significant PCE decay attributed to a faster degradation at the interface between PEDOT:PSS and perovskite (Figure 11).[36] Interestingly, compared to PEDOT:PSS and PDI, devices fabricated with PDAI working as HTL did not show any evidence of degradation, indicating a high stability. In agreement with the aforementioned statements, this can be attributed to the protective effect of the self-assembled HTL, whose robust hydrogen-bonded network preserves the perovskite solar cell from degradation.

3. Conclusion

In summary, we have evaluated two novel π-conjugated small molecules, PDI and PDAI, for use as HTLs in narrow-bandgap PSCs. Both materials are synthesized in a simple two-step procedure. It is found that such HTLs are suitable to obtain good quality films of the $FA_{0.66}MA_{0.34}Pb_{0.5}Sn_{0.5}I_3$ deposited on top. Compared to PDI, PDAI is more robust against solution-processed perovskite films favored by its hydrogen-bond-directed self-assembled arrangement. As a result, the devices with PDAI show much-improved reproducibility. Compared to PEDOT:PSS, both PDAI and PDI exhibit similar charge transport properties in narrow-bandgap solar cells, resulting in a comparable V_{OC} and FF. In both cases, the use of ultrathin HTLs enhances the J_{SC} by changing the optical interference and reducing parasitic absorption from the PEDOT:PSS layer. Replacing the PEDOT:PSS HTL also significantly improves the shelf life of narrow-bandgap solar cells. These results encourage further research to explore new self-assembled molecular materials as interfacial layers in perovskite-based photovoltaics.

Supporting Information

Supporting Information is available from the Wiley Online Library or from the author.

Acknowledgements

P.G. and J.W. contributed equally to this work. The authors thank Dr. Junyu Li for GIWAX measurements, Kunal Datta for XRD measurements, Bas van Gorkom for sub-bandgap EQE experiments, Tom van der Pol for optical simulations, Riccardo Ollearo for transient photocurrent measurements, and Antonio García for DFT calculations. The authors acknowledge the financial support from the Ministry of Science, Innovation and Universities (Project RTI2018-101092-B-I00) and Programa Estatal de Fomento de la Investigación Científica y Técnica de Excelencia (RED2018-102815-T). The authors are also grateful to Fundación Séneca–Agencia de Ciencia y Tecnología de la Región de Murcia for funding the Project 20959/PI/18 and M.M.-M.'s postdoctoral contract from the "Saavedra Fajardo Program" (20406/SF/17). Further funding was received from the Netherlands Organization for Scientific Research via the NWO Spinoza grant and from the Ministry of Education, Culture and Science (Gravity program 024.001.035).

Conflict of Interest

The authors declare no conflict of interest.

Data Availability Statement

Research data are not shared.

Keywords

hole transporting materials, hydrogen-bonded materials, Pb–Sn perovskite solar cells, self-assembly

Received: June 26, 2021
Revised: August 20, 2021
Published online: September 8, 2021

[1] M. A. Green, E. D. Dunlop, J. Hohl-Ebinger, M. Yoshita, N. Kopidakis, X. Hao, *Prog. Photovoltaics Res. Appl.* **2020**, *28*, 629.
[2] N. Moody, S. Sesena, D. W. deQuilettes, B. D. Dou, R. Swartwout, J. T. Buchman, A. Johnson, U. Eze, R. Brenes, M. Johnston, C. L. Haynes, V. Bulović, M. G. Bawendi, *Joule* **2020**, *4*, 970.
[3] Q. Chen, J. Wu, J. T. Matondo, L. Bai, D. M. Maurice, M. Guli, *Sol. RRL* **2020**, *4*, 2000584.
[4] G. Nasti, A. Abate, *Adv. Energy Mater.* **2020**, *10*, 1902467.
[5] a) A. M. Igual-Muñoz, A. Castillo, C. Dreessen, P. P. Boix, H. J. Bolink, *ACS Appl. Energy Mater.* **2020**, *3*, 2755; b) J. Wang, K. Datta, J. Li, M. A. Verheijen, D. Zhang, M. M. Wienk, R. A. J. Janssen, *Adv. Energy Mater.* **2020**, *10*, 2000566; c) H. L. Zhu, H. Lin, Z. Song, Z. Wang, F. Ye, H. Zhang, W. J. Yin, Y. Yan, W. C. H. Choy, *ACS Nano* **2019**, *13*, 11800.
[6] S. Gu, R. Lin, Q. Han, Y. Gao, H. Tan, J. Zhu, *Adv. Mater.* **2020**, *32*, 1907392.
[7] S. Rühle, *Sol. Energy* **2016**, *130*, 139.
[8] S. Gu, R. Lin, Q. Han, Y. Gao, H. Tan, J. Zhu, *Adv. Mater.* **2020**, *32*, 1907392.
[9] a) R. Lin, K. Xiao, Z. Qin, Q. Han, C. Zhang, M. Wei, M. I. Saidaminov, Y. Gao, J. Xu, M. Xiao, A. Li, J. Zhu, E. H. Sargent, H. Tan, *Nat. Energy* **2019**, *4*, 864; b) Z. Yang, Z. Yu, H. Wei, X. Xiao, Z. Ni, B. Chen, Y. Deng, S. N. Habisreutinger, X. Chen, K. Wang, J. Zhao, P. N. Rudd, J. J. Berry, M. C. Beard, J. Huang, *Nat. Commun.* **2019**, *10*, 4498; c) J. H. Tong, Z. N. Song, D. H. Kim, X. H. Chen, C. Chen, A. F. Palmstrom, P. F. Ndione, M. O. Reese, S. P. Dunfield, O. G. Reid, J. Liu, F. Zhang, S. P. Harvey, Z. Li, S. T. Christensen, G. Teeter, D. W. Zhao, M. M. Al-Jassim, M. F. A. M. van Hest, M. C. Beard, S. E. Shaheen, J. J. Berry, Y. Yan, K. Zhu, *Science* **2019**, *364*, 475.
[10] M. T. Klug, R. L. Milot, J. B. Patel, T. Green, H. C. Sansom, M. D. Farrar, A. J. Ramadan, S. Martani, Z. Wang, B. Wenger, J. M. Ball, L. Langshaw, A. Petrozza, M. B. Johnston, L. M. Herz, H. J. Snaith, *Energy Environ. Sci.* **2020**, *13*, 1776.
[11] J. Cao, F. Yan, *Energy Environ. Sci.* **2021**, *14*, 1286.
[12] a) R. Prasanna, T. Leijtens, S. P. Dunfield, J. A. Raiford, E. J. Wolf, S. A. Swifter, J. Werner, G. E. Eperon, C. de Paula, A. F. Palmstrom, C. C. Boyd, M. F. A. M. van Hest, S. F. Bent, G. Teeter, J. J. Berry, M. D. McGehee, *Nat. Energy* **2019**, *4*, 939; b) J. Werner, T. Moot, T. A. Gossett, I. E. Gould, A. F. Palmstrom, E. J. Wolf, C. C. Boyd, M. F. A. M. van Hest, J. M. Luther, J. J. Berry, M. D. McGehee, *ACS Energy Lett.* **2020**, *5*, 1215.
[13] a) Z. Yu, Z. Yang, Z. Ni, Y. Shao, B. Chen, Y. Lin, H. Wei, Z. J. Yu, Z. Holman, J. Huang, *Nat. Energy* **2020**, *5*, 657; b) D. Zhao, C. Chen, C. Wang, M. M. Junda, Z. Song, C. R. Grice, Y. Yu, C. Li, B. Subedi, N. J. Podraza, X. Zhao, G. Fang, R.-G. Xiong, K. Zhu, Y. Yan, *Nat. Energy* **2018**, *3*, 1093.
[14] G. Xu, P. Bi, S. Wang, R. Xue, J. Zhang, H. Chen, W. Chen, X. Hao, Y. Li, Y. Li, *Adv. Funct. Mater.* **2018**, *28*, 1804427.
[15] H. Tang, Y. Shang, W. Zhou, Z. Peng, Z. Ning, *Sol. RRL* **2019**, *3*, 1800256.
[16] J. Song, W. Hu, Z. Li, X.-F. Wang, W. Tian, *Sol. Energy Mater. Sol. Cells* **2020**, *207*, 110351.
[17] A. M. Igual-Muñoz, J. Ávila, P. P. Boix, H. J. Bolink, *Sol. RRL* **2020**, *4*, 1900283.
[18] S. Shao, Y. Cui, H. Duim, X. Qiu, J. Dong, G. H. ten Brink, G. Portale, R. C. Chiechi, S. Zhang, J. Hou, M. A. Loi, *Adv. Mater.* **2018**, *30*, 1803703.
[19] M. Más-Montoya, P. Gómez, D. Curiel, I. da Silva, J. Wang, R. A. J. Janssen, *Chem. Eur. J.* **2020**, *26*, 10276.
[20] P. Gómez, S. Georgakopoulos, M. Más-Montoya, J. Cerdá, J. Pérez, E. Ortí, J. Aragó, D. Curiel, *ACS Appl. Mater. Interfaces* **2021**, *13*, 8620.
[21] R. Dorel, C. P. Grugel, A. M. Haydl, *Angew. Chem. Int. Ed.* **2019**, *58*, 17118.
[22] Y. Hashimoto, K. Shudo, *Chem. Pharm. Bull.* **1984**, *32*, 1992.
[23] J. K. Laha, S. M. Barolo, R. A. Rossi, G. D. Cuny, *J. Org. Chem.* **2011**, *76*, 6421.
[24] a) I. Salzmann, S. Duhm, G. Heimel, M. Oehzelt, R. Kniprath, R. L. Johnson, J. P. Rabe, N. Koch, *J. Am. Chem. Soc.* **2008**, *130*, 12870; b) G. Heimel, I. Salzmann, S. Duhm, N. Koch, *Chem. Mater.* **2011**, *23*, 359; c) S. Duhm, G. Heimel, I. Salzmann, H. Glowatzki, R. L. Johnson, A. Vollmer, J. P. Rabe, N. Koch, *Nat. Mater.* **2008**, *7*, 326; d) G. D'Avino, L. Muccioli, F. Castet, C. Poelking, D. Andrienko, Z. G. Soos, J. Cornil, D. Beljonne, *J. Phys.: Condens. Matter* **2016**, *28*, 433002.
[25] B. J. Bruijnaers, E. Schiepers, C. H. L. Weijtens, S. C. J. Meskers, M. M. Wienk, R. A. J. Janssen, *J. Mater. Chem. A* **2018**, *6*, 6882.
[26] H. Yoshida, *J. Phys. Chem. C* **2014**, *118*, 24377.
[27] H. Yoshida, *J. Phys. Chem. C* **2015**, *119*, 24459.
[28] Q. Shi, C. Zhu, M. H. Engelhard, D. Du, Y. Lin, *RSC Adv.* **2017**, *7*, 6303.
[29] J. Wang, K. Datta, J. Li, M. A. Verheijen, D. Zhang, M. M. Wienk, R. A. J. Janssen, *Adv. Energy Mater.* **2020**, *10*, 2000566.
[30] J. Lu, W. Feng, G. Mei, J. Sun, C. Yan, D. Zhang, K. Lin, D. Wu, K. Wang, Z. Wei, *Adv. Sci.* **2020**, *7*, 2000689.
[31] M. Stolterfoht, P. Caprioglio, C. M. Wolff, J. A. Márquez, J. Nordmann, S. Zhang, D. Rothhardt, U. Hörmann, Y. Amir, A. Redinger, L. Kegelmann, F. Zu, S. Albrecht, N. Koch,

T. Kirchartz, M. Saliba, T. Unold, D. Neher, *Energy Environ. Sci.* **2019**, *12*, 2778.
[32] Z. Li, C. R. McNeill, *J. Appl. Phys.* **2011**, *109*, 074513.
[33] W. Tress, M. Yavari, K. Domanski, P. Yadav, B. Niesen, J. P. Correa Baena, A. Hagfeldt, M. Graetzel, *Energy Environ. Sci.* **2018**, *11*, 151.
[34] Y. Shao, Z. Xiao, C. Bi, Y. Yuan, J. Huang, *Nat. Commun.* **2014**, *5*, 5784.
[35] A. Al-Ashouri, A. Magomedov, M. Roß, M. Jošt, M. Talaikis, G. Chistiakova, T. Bertram, J. A. Márquez, E. Köhnen, E. Kasparavičius, S. Levcenco, L. Gil-Escrig, C. J. Hages, R. Schlatmann, B. Rech, T. Malinauskas, T. Unold, C. A. Kaufmann, L. Korte, G. Niaura, V. Getautis, S. Albrecht, *Energy Environ. Sci.* **2019**, *12*, 3356.
[36] R. Prasanna, T. Leijtens, S. P. Dunfield, J. A. Raiford, E. J. Wolf, S. A. Swifter, J. Werner, G. E. Eperon, C. de Paula, A. F. Palmstrom, C. C. Boyd, M. F. A. M. van Hest, S. F. Bent, G. Teeter, J. J. Berry, M. D. McGehee, *Nat. Energy* **2019**, *4*, 939.